LETTERS
PUBLISHED ONLINE: 19 SEPTEMBER 2010 | DOI: 10.1038/NNANO.2010.176
nature nanotechnology

Optical rectification and field enhancement in a plasmonic nanogap

Daniel R. Ward[1], Falco Hüser[2], Fabian Pauly[2], Juan Carlos Cuevas[3] and Douglas Natelson[1,4]*

Metal nanostructures act as powerful optical antennas[1,2] because collective modes of the electron fluid in the metal are excited when light strikes the surface of the nanostructure. These excitations, known as plasmons, can have evanescent electromagnetic fields that are orders of magnitude larger than the incident electromagnetic field. The largest field enhancements often occur in nanogaps between plasmonically active nanostructures[3,4], but it is extremely challenging to measure the fields in such gaps directly. These enhanced fields have applications in surface-enhanced spectroscopies[5–7], nonlinear optics[1,8–10] and nanophotonics[11–15]. Here we show that nonlinear tunnelling conduction between gold electrodes separated by a subnanometre gap leads to optical rectification, producing a d.c. photocurrent when the gap is illuminated. Comparing this photocurrent with low-frequency conduction measurements, we determine the optical frequency voltage across the tunnelling region of the nanogap, and also the enhancement of the electric field in the tunnelling region, as a function of gap size. The measured field enhancements exceed 1,000, consistent with estimates from surface-enhanced Raman measurements[16–18]. Our results highlight the need for more realistic theoretical approaches that are able to model the electromagnetic response of metal nanostructures on scales ranging from the free-space wavelength, λ, down to $\sim\lambda$/1,000, and for experiments with new materials, different wavelengths and different incident polarizations.

The probability of an electron being able to tunnel across a small gap decays exponentially with distance; hence, electron tunnelling can be used to measure distances with high precision, as in the case of scanning tunnelling microscopy (STM). Moreover, nonlinearity in tunnelling conduction can convert the optical frequency response of the metal into a d.c. current. This rectification process, originally proposed as a means of inferring the tunnelling time[19], allows the optical frequency voltage difference across the tunnelling gap to be determined. Evidence for microwave rectification[20] and optical rectification[21,22] has been reported for STM experiments, but thermal and surface photovoltage effects[20] complicate interpretation of the optical data.

Suppose that the d.c. two-terminal current–voltage characteristics of some object are $I(V_{dc})$, where I is the current and V_{dc} is the d.c. voltage bias. If we add a small a.c. voltage bias, $V_{ac}\cos(\omega t)$, to V_{dc}, and if the underlying conduction mechanism remains valid at some frequency scale 2ω, then we would expect[20] the total current to be

$$I \approx I(V_{dc}) + \left.\frac{\partial I}{\partial V}\right|_{V_{dc}} V_{ac}\cos(\omega t) + \left.\frac{1}{2}\frac{\partial^2 I}{\partial V^2}\right|_{V_{dc}} V_{ac}^2\cos^2(\omega t) + \cdots$$
$$\approx \left[I(V_{dc}) + \left.\frac{1}{4}\frac{\partial^2 I}{\partial V^2}\right|_{V_{dc}} V_{ac}^2\right] + \left.\frac{\partial I}{\partial V}\right|_{V_{dc}} V_{ac}\cos(\omega t) - \left.\frac{1}{4}\frac{\partial^2 I}{\partial V^2}\right|_{V_{dc}} V_{ac}^2\cos(2\omega t) + \cdots \quad (1)$$

In addition to $I(V_{dc})$, in the presence of the a.c. excitation there is a rectified d.c. current proportional to the nonlinearity of the conductance and the square of the a.c. excitation amplitude. As demonstrated[20] using STM and microwave irradiation, one may use a low-frequency a.c. voltage and lock-in amplifier to measure $\partial^2 I/\partial V^2$ using the second harmonic of the a.c. voltage. Using lock-in techniques to measure the d.c. current due to microwave irradiation of a known microwave voltage, others have found quantitative agreement between the rectified microwave current and the expectations of equation (1)[20].

In the optical case, in the limit that this rectification picture is valid, one would expect the radiation-induced a.c. response of the metal to lead to a photocurrent, I_{photo}, in addition to the usual d.c. current, $I(V_{dc})$. One may then infer the local, radiation-induced a.c. voltage, V_{opt}, by comparing I_{photo} and detailed low-frequency characterization of the conductance. In a tunnel junction, the differential conductance, $\partial I/\partial V$, at zero bias can be related to the interelectrode separation through the exponential decay of the conductance with increasing distance, $G \approx \exp(-\beta(d - d_0))$. Here d is the internuclear distance between closest atoms, d_0 is the size of the metal lattice constant, and β is the attenuation factor. The average local electric field at the closest interelectrode separation, $V_{opt}/(d - d_0)$, may then be inferred and compared with the incident field known from the incident optical intensity, giving a quantitative measure of the field enhancement due to the metal optical response. The V_{opt} inferred experimentally is that experienced by the optical frequency tunnelling electrons. Because both V_{opt} and $d - d_0$ are found from tunnelling, which is a very local process, this is self-consistent. This means that voltage drops within the metal far from the tunnelling gap are not relevant to the processes being studied, but, as we discuss in the Supplementary Information, there are subtleties to consider, including the role of screening in the metal and the locality of the tunnelling process.

A quantum treatment of radiation interacting with a nanoscale junction involves photon-assisted tunnelling[23] and has been applied to atomic-scale metal contacts[24,25]. When a junction is illuminated with radiation of energy $\hbar\omega$, the junction's plasmonic response results in an a.c. voltage, V_{opt}, at frequency ω across the junction. Following the Tien–Gordon approach[26], the quantum correction to the d.c. current induced by the radiation in the limit of small a.c. amplitudes ($eV_{opt} \ll \hbar\omega$) is given by

$$I(V_{dc}, V_{opt}, \omega) - I(V_{dc}) = \frac{1}{4}V_{opt}^2\left[\frac{I(V_{dc} + \hbar\omega/e) - 2I(V_{dc}) + I(V_{dc} - \hbar\omega/e)}{(\hbar\omega/e)^2}\right] \quad (2)$$

If the tunnelling nonlinearity is small on the voltage scale $\hbar\omega/e$, this expression reduces to equation (1), with V_{opt} playing the role of V_{ac}.

[1]Department of Physics and Astronomy, Rice University, 6100 Main Street, Houston, Texas 77005, USA, [2]Institut für Theoretische Festkörperphysik, Karlsruhe Institute of Technology, 76131 Karlsruhe, Germany, [3]Departamento de Física Teórica de la Materia Condensada, Universidad Autónoma de Madrid, 28049 Madrid, Spain, [4]Department of Electrical and Computer Engineering, Rice University, 6100 Main Street, Houston, Texas 77005, USA. *e-mail: natelson@rice.edu

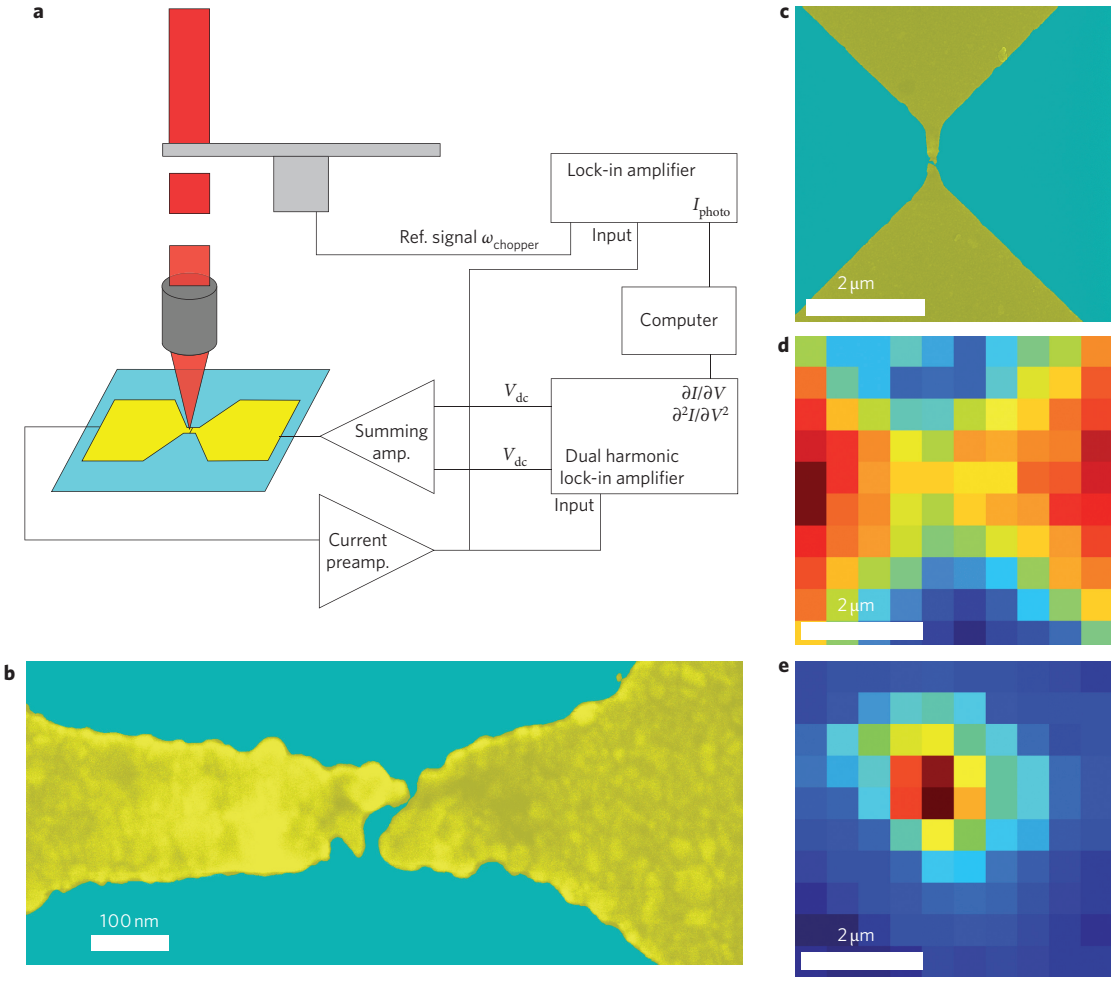

Figure 1 | Measurement approach and layout. a, Schematic diagram of electrical characterization measurement. **b**, Colourized scanning electron microscope (SEM) image of a typical nanogap device. The actual tunnelling gap is not resolvable by SEM. **c**, Larger SEM view of electrodes and nanogap. **d**,**e**, False-colour maps of the silicon Raman line (**d**) and the photocurrent (**e**) for the device shown in **c**. In **d** blue indicates a weak silicon signal, thus indicating the location of the gold electrodes. In **e**, the colour bar runs from red (20 nA) to blue (0 nA). The photocurrent is clearly localized to the nanogap, to within optical resolution.

This occurs when the transmittance of the junction $\tau(E)$ is smooth as a function of energy near the Fermi level of the leads, E_F, throughout $E_F \pm \hbar\omega$.

Details of the sample fabrication and the optical and electronic measurements are described in the Methods. Nanogaps are formed in the gold constrictions by electromigration[27]. The electromigration process is stopped once the zero-bias d.c. conductance of the gaps is less than $2e^2/h \equiv G_0$. Typical conductances in this experiment are of the order of $0.6G_0$ to $0.016G_0$, indicating average gaps, $d - d_0$, ranging from 0.03 to 0.23 nm. Figure 1 shows the measurement system and basic characterization of a representative nanogap. The illumination wavelength is 785 nm, with a peak intensity of 22.6 kW cm^{-2}, and measurements are performed in vacuum at 80 K.

The d.c. I–V characteristics of the samples after electromigration are weakly nonlinear, with no sharp features, as expected for clean vacuum tunnel junctions. These junctions, ideally devoid of molecules, show no molecular surface-enhanced Raman scattering signal[16,17], as expected. Figure 2 shows representative $\partial^2 I/\partial V^2$ versus V_{dc} curves and simultaneously recorded I_{photo} versus V_{dc} data for three different samples, acquired with the beam fixed over the nanogap. For each set of curves shown, the amplitude of V_{ac} has been set such that $(1/4)V_{ac}^2\partial^2 I/\partial V^2$ and I_{photo} are of the same amplitude. The fact that I_{photo} is directly proportional to $\partial^2 I/\partial V^2$ consistently over the whole d.c. bias range, including through the V_{dc} where both change sign, strongly implies that the photocurrent originates from the rectification mechanism. In this case, when $(1/4)V_{ac}^2\partial^2 I/\partial V^2 = I_{photo}$, this implies $V_{ac} = V_{opt}$, where V_{opt} is the amplitude of the optically induced voltage between the two electrodes that oscillates at $\omega/2\pi = 3.8 \times 10^{14}$ Hz. When the rectification mechanism is responsible for the photocurrent, comparison with low-frequency electrical measurements gives a means of quantitatively assessing the plasmon-induced a.c. voltage across the nanoscale interelectrode gap. As a consistency check, we have mapped the optically rectified current, I_{photo}, at fixed V_{dc} (while monitoring I, $\partial I/\partial V$ and $\partial^2 I/\partial V^2$, to ensure junction stability during the mapping procedure). As shown in Fig. 1e, I_{photo} is only produced when the gap itself is illuminated.

Previous tunnelling optical rectification experiments have been hampered by thermal voltages and thermal expansion. We do not expect thermal voltages in our experiment because the device is a comparatively symmetric design, and with a centred laser spot there should be no temperature gradient between the electrodes, even in the presence of minor structural asymmetries. The macroscale unilluminated parts of the electrodes also act as thermal sinks. Differential thermal voltages caused by asymmetry of illumination would show up as systematic trends in I_{photo} as a function of

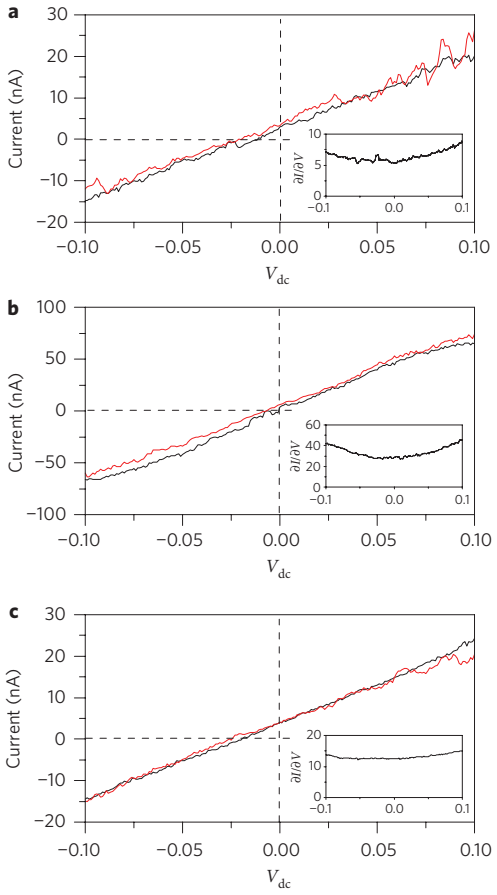

Figure 2 | Demonstration of optical rectification. a–c, Photocurrent (red, I_{photo}) and $(1/4)V_{ac}^2\partial^2 I/\partial V^2$ (black) as a function of V_{dc} for three different samples. The shared shapes of these curves, including changes of sign, demonstrate that the photocurrent arises from the rectification process. Note the differing current scales for the three devices. The different conductances and nonlinearities presumably result from microscopic details of the electrode surfaces and geometry. Insets: conductance in units of $\mu A\,V^{-1}$ for each device. The gap distances derived from tunnelling measurements are 1.4, 0.44 and 0.92 Å. Inferred V_{opt} values are 30, 25 and 33 mV, with uncertainties of 10%. Inferred electromagnetic fields and field enhancements are 2.1×10^8 V m^{-1} and 718 for **a**, 5.7×10^8 V m^{-1} and 1,940 for **b**, and 3.6×10^8 V m^{-1} and 1,230 for **c**.

laser position, and Fig. 1e shows no such trends. Thermal expansion should be irrelevant, because the electrodes are intimately mechanically coupled to the substrate, with essentially no unsupported electrode material. To check for thermal effects, we looked for changes in $\partial I/\partial V$ at $\omega_{chopper}$, because any laser-induced expansion should modulate the interelectrode gap and thus the conductance. No measurable effect was found to better than the 10^{-4} level.

Optical rectification is further supported by measurements of I_{photo} versus incident laser power. In Fig. 3 we see the expected linear dependence. The best-fit line has a slope of 0.37 nA kW^{-1} cm^2. Further, as expected, V_{dc} can be selected so that $\partial^2 I/\partial V^2$ is zero (not always at $V_{dc} = 0$), and at that bias I_{photo} measurements show no detectable current.

The validity of the rectification picture is not completely obvious for this system *a priori*. Detailed calculations of the transmission as a function of energy, as shown in Fig. 4, demonstrate that for this particular material and illuminating wavelength, corrections to the classical rectification picture should be relatively small. At higher d.c. biases (>100 mV, not shown), we often observe deviations of the photocurrent from the measured $(1/4)V_{ac}^2\partial^2 I/\partial V^2$.

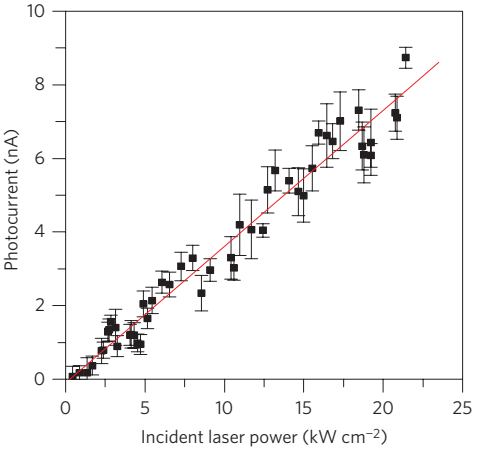

Figure 3 | Further evidence for optical rectification. Rectified photocurrent, I_{photo}, as a function of incident laser power. Error bars indicate one standard deviation of the I_{photo} measurements at each laser power. Linear power dependence (see text) was found by a weighted least-squares fit (red line).

To infer the nanogap size from the conductance measurements, we performed theoretical simulations of the breaking process of gold atomic contacts. In these simulations, we used density functional theory to determine the geometry of the junctions as well as to compute the transport properties within the Landauer approach, as detailed in ref. 28. In this approach the low-temperature linear conductance is given by $G = G_0\tau(E_F)$, where $\tau(E_F)$ is the transmission of the contact evaluated at the Fermi energy, E_F. To simulate the rupture of the gold nanowires, we start out with a single-atom contact (Fig. 4a). We separate the electrodes stepwise, re-optimize the geometry in every step and compute the corresponding conductance. As in Fig. 4c, in the relevant range, the linear conductance decays exponentially with an attenuation factor of $\beta \approx 1.8$ Å^{-1}. Extensive simulations (see Supplementary Information) show that this exponent varies within 10%, depending on the geometry of the contact.

Using $\beta = 1.85$ Å^{-1} (averaged over different junction structures), the interelectrode gap, $d - d_0$, can be found from the measured $\partial I/\partial V$. With this and the inferred V_{opt}, the enhanced electric field local to the tunnelling gap may be determined. The experimental uncertainty in V_{opt} is ~5%, based on the comparisons shown in Fig. 2. The experimental uncertainty in the tunnelling conductance at zero bias is ~1%. The dominant uncertainty in the inferred interelectrode separation is systematic, owing to variation of β with the morphology of metal surfaces. Assuming that $d - d_0$ is the appropriate scale for computing the local electric field, for the samples in Fig. 2, the optical electric fields (r.m.s., root mean square) are 2.1×10^8, 5.7×10^8 and 3.6×10^8 V m^{-1}. On the basis of Gaussian beam shape and incident power, the free-space incident r.m.s. field is 2.9×10^5 V m^{-1}. Therefore, we determine the local enhancement factors of the electric field as 718, 1,940 and 1,230. These very large enhancements exceed expectations from idealized finite difference time domain (FDTD) calculations[16] for wider gaps, and are consistent with observations of single-molecule Raman emission in such junctions[17,18]. At sufficiently high electric field strengths the gap geometry can become unstable. We believe that this is why the I–V curves of some devices exhibit instabilities. In the absence of the optical field or at considerably reduced incident laser fluences, the I–V curves are very stable.

Our calculations clarify why the classical rectification formula works in our case. The transmission function (Fig. 4d) of these gold contacts shows only a weak energy dependence around the Fermi energy in the interval $[E_F - \hbar\omega, E_F + \hbar\omega]$. This indicates that the quantum result of equation (2) reduces to the classical rectification formula of equation (1). This smoothness is because

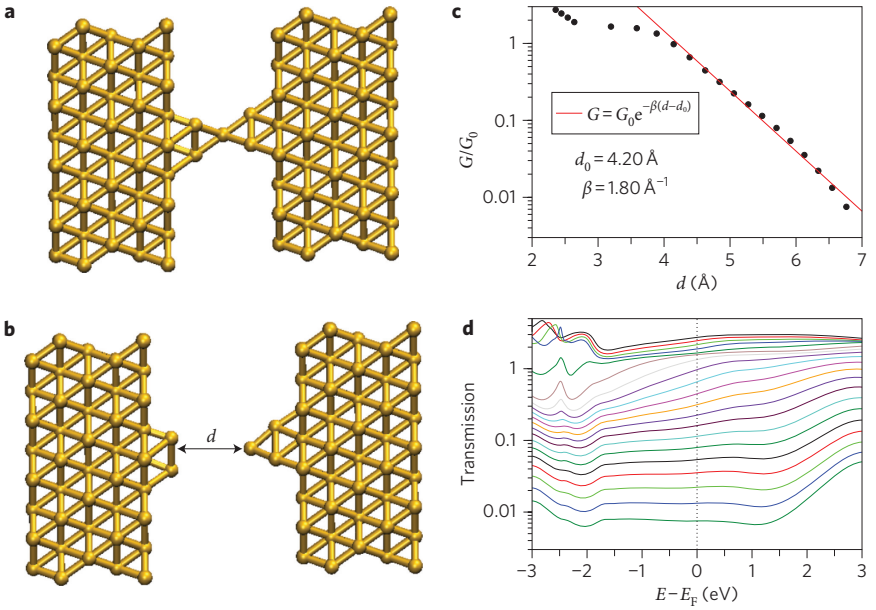

Figure 4 | Theoretical basis for validity of rectification. a, Geometry considered in the theoretical analysis of the distance dependence of linear conductance. We start with a single-atom contact grown along the ⟨111⟩ direction. **b**, Stretched geometry with a distance d between the gold tips. **c**, Calculated linear conductance as a function of d (circles). The solid line shows the fit to the exponential function $G = G_0 \exp[-\beta(d - d_0)]$. The fit parameters are indicated in the graph. **d** Zero-bias transmission as a function of the energy for the different geometries of **c**, with d increasing from top to bottom. Note the logarithmic vertical axis, and that the transmission remains a smooth function of energy over a broad range around the Fermi level.

transport in the gold contacts is dominated by the *s* atomic orbitals, with a relatively flat density of states. Similar physics should therefore be expected in other *s*-valent metals, such as silver.

In several devices, conductance decreased over the course of hours of measurements, as the metal electrodes rearranged themselves, allowing us to track variations in V_{opt} (and inferred enhanced electric field) as a function of interelectrode separation (Fig. 5). Despite device-to-device variability, the general trend shows increasing enhancement with decreasing $d - d_0$. This trend is slower than $1/(d - d_0)$ and weaker than classical expectations[29]. Such a comparatively weak increase in enhancement at low $d - d_0$ is qualitatively consistent with calculations that examine quantum tunnelling corrections to plasmonic enhancements in nanoparticle dimers[29,30]. However, those calculations predict an actual decrease in enhancement when $d - d_0$ is small enough that interelectrode conductance is strong enough to short out the nanogap plasmons. From our data and previous observations[17], this decrease in enhancement does not occur in gold nanojunctions until the interelectrode conductance exceeds G_0. Our measurements highlight the need for detailed, realistic theoretical treatments of these nanostructures, incorporating optical interactions, quantum effects and dynamical screening.

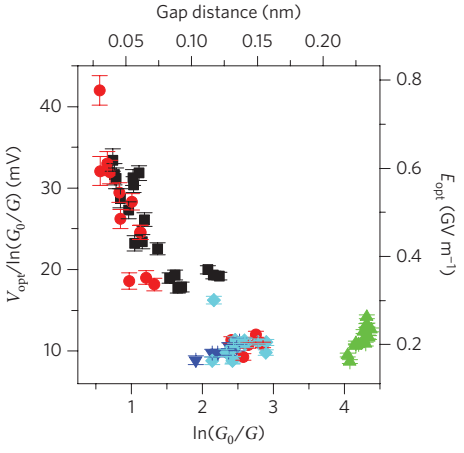

Figure 5 | Field (right axis) at the tunnelling region as a function of gap distance (top axis) for five devices (shown in different colours) measured a number of times at 80 K. The gap distance (and therefore the enhanced field) changes as the gap geometry evolves over the course of repeated measurements. The field and gap distance are derived from measurements of the conductance (bottom axis shows $\ln(G_0/G)$) and optical frequency voltage (left axis shows V_{opt} normalized by $\ln(G_0/G)$), based on the assumption that $d - d_0$ is the relevant scale over which V_{opt} falls, and $\beta = 1.85$ Å^{-1}. Error bars result from the statistical uncertainty in V_{opt} and ln G.

Methods

Samples were fabricated using standard electron-beam lithography techniques to define metal (1 nm titanium/15 nm gold) constrictions 100 nm in width and 600 nm in length between larger contact pads, on highly doped n-type silicon substrates covered with 200 nm of thermally grown SiO_2. After cleaning in oxygen plasma, devices were wirebonded to a chip carrier, installed in a microscope cryostat and cooled to 80 K.

After electromigration the sample was illuminated with a 785 nm laser focused to a Gaussian spot with a FWHM of 1.9 μm and a peak intensity of 22.6 kW cm^{-2}. The laser was rastered over the sample surface and the Raman response of the silicon substrate was measured at 520 cm^{-1}. The gold electrodes attenuate silicon Raman emission, allowing precise mapping of the nanogap structure, as shown in Fig. 1d. Once the nanogap was located by means of the silicon Raman map, the laser was centred over the gap. The laser polarization was aligned along the original constriction.

The sample was electrically characterized by means of the apparatus presented in Fig. 1a using two lock-in amplifiers and a current amplifier. The first lock-in amplifier applies an a.c. excitation (V_{ac} cos $\omega_1 t$) to the sample at $\omega_1 = 2.0$ kHz and simultaneously measures the first ($\propto \partial I/\partial V$) and second harmonic response ($=(1/4)V_{ac}^2 \partial^2 I/\partial V^2$) of the nanogap to this excitation. There is no measurable change in either of these responses when the laser illumination is added or removed. The first harmonic response is essentially in phase with the ω_1 reference. The second harmonic response is phased relative to the $2\omega_1$ reference by 180° as defined by the lock-in, such that the integrated $\partial^2 I/\partial V^2$ signal gives back the $\partial I/\partial V$ signal. The second lock-in amplifier is referenced to (and in phase with) an optical chopper at $\omega_{chopper} = 232$ Hz and measures the current generated due to the radiation (I_{photo}). A summing amplifier is used to add a d.c. voltage V_{dc} to V_{ac}. With this arrangement, $I(V_{dc})$, $\partial I/\partial V$, $\partial^2 I/\partial V^2$ and I_{photo} as a function of V_{dc} can be measured simultaneously.

Received 11 June 2010; accepted 27 July 2010;
published online 19 September 2010

References

1. Mühlschlegel, P., Eisler, H., Martin, O., Hecht, B. & Pohl, D. Resonant optical antennas. *Science* **308,** 1607–1609 (2005).
2. Schuck, P. J., Fromm, D. P., Sundaramurthy, A., Kino, G. S. & Moerner, W. E. Improving the mismatch between light and nanoscale objects with gold bowtie nanoantennas. *Phys. Rev. Lett.* **94,** 017402 (2005).
3. Jiang, J., Bosnick, K., Maillard, M. & Brus, L. Single molecule Raman spectroscopy at the junctions of large Ag nanocrystals. *J. Phys. Chem. B* **107,** 9964–9972 (2003).
4. Li, K., Stockman, M. I. & Bergman, D. J. Self-similar chain of metal nanospheres as an efficient nanolens. *Phys. Rev. Lett.* **91,** 227402 (2003).
5. Otto, A., Mrozek, I., Grabhorn, H. & Akemann, W. Surface enhanced Raman scattering. *J. Phys. Condens. Matter* **4,** 1143–1212 (1992).
6. Hartstein, A., Kirtley, J. R. & Tsang, J. C. Enhancement of the infrared absorption from molecular monolayers with thin metal overlayers. *Phys. Rev. Lett.* **45,** 201–204 (1980).
7. Fort, E. & Gresillon, S. Surface enhanced fluorescence. *J. Phys. D.* **41,** 013001 (2008).
8. Danckwerts, M. & Novotny, L. Optical frequency mixing at coupled gold nanoparticles. *Phys. Rev. Lett.* **98,** 026104 (2007).
9. Bouhelier, A., Beversluis, M. R. & Novotny, L. Characterization of nanoplasmonic structures by locally excited photoluminescence. *Appl. Phys. Lett.* **83,** 5041–5043 (2003).
10. Ghenuche, P., Cherukulappurath, S., Taminiau, T. H., van Hulst, N. F. & Quidant, R. Spectroscopic mode mapping of resonant plasmon nanoantennas. *Phys. Rev. Lett.* **101,** 116805 (2008).
11. Akimov, A. V. *et al.* Generation of single optical plasmons in metallic nanowires coupled to quantum dots. *Nature* **450,** 402–406 (2007).
12. Dionne, J. A., Diest, K., Sweatlock, L. A. & Atwater, H. A. PlasMOStor: a metal-oxide-Si field effect plasmonic modulator. *Nano Lett.* **9,** 897–902 (2009).
13. Yu, N. *et al.* Plasmonic quantum cascade laser antenna. *Appl. Phys. Lett.* **91,** 173113 (2007).
14. Oulton, R. F. *et al.* Plasmon lasers at deep subwavelength scale. *Nature* **461,** 629–632 (2009).
15. Noginov, M. A. *et al.* Demonstration of a spaser-based nanolaser. *Nature* **460,** 1110–1112 (2009).
16. Ward, D. R. *et al.* Electromigrated nanoscale gaps for surface-enhanced Raman spectroscopy. *Nano Lett.* **7,** 1396–1400 (2007).
17. Ward, D. R. *et al.* Simultaneous measurements of electronic conduction and Raman response in molecular junctions. *Nano Lett.* **8,** 919–924 (2008).
18. Ward, D. R., Scott, G. D., Keane, Z. K., Halas, N. J. & Natelson, D. Electronic and optical properties of electromigrated molecular junctions. *J. Phys. Condens. Matter* **20,** 374118 (2008).
19. Cutler, P. H. *et al.* Proposed use of a scanning-tunnelling-microscope tunnel junction for the measurement of a tunnelling time. *Phys. Rev. B* **35,** 7774–7775 (1987).
20. Tu, X. W., Lee, J. H. & Ho, W. Atomic-scale rectification at microwave frequency. *J. Chem. Phys.* **124,** 021105 (2006).
21. Nguyen, H. Q. *et al.* Mechanisms of current rectification in an STM tunnel junction and the measurement of an operational tunnelling time. *IEEE Trans. Elect. Dev.* **36,** 2671–2678 (1989).
22. Bragas, A. V., Landi, S. M. & Martínez, O. E. Laser field enhancement at the scanning tunnelling microscope junction measured by optical rectification. *Appl. Phys. Lett.* **72,** 2075–2077 (1998).
23. Viljas, J. K. & Cuevas, J. C. Role of electronic structure in photoassisted transport through atomic-sized contacts. *Phys. Rev. B* **75,** 075406 (2007).
24. Guhr, D. C. *et al.* Influence of laser light on electronic transport through atomic-size contacts. *Phys. Rev. Lett.* **99,** 086801 (2007).
25. Ittah, N., Noy, G., Yutsis, I. & Selzer, Y. Measurement of electronic transport through $1G_0$ gold contacts under laser irradiation. *Nano Lett.* **9,** 1615–1620 (2009).
26. Tien, P. K. & Gordon, J. P. Multiphoton process observed in the interaction of microwave fields with the tunnelling between superconductor films. *Phys. Rev.* **129,** 647–651 (1963).
27. Park, H., Lim, A. K. L., Alivisatos, A. P., Park, J. & McEuen, P. L. Fabrication of metallic electrodes with nanometer separation. *Appl. Phys. Lett.* **75,** 301–303 (1999).
28. Pauly, F. *et al.* Cluster-based density-functional approach to quantum transport through molecular and atomic contacts. *New J. Phys.* **10,** 125019 (2008).
29. Zuloaga, J., Prodan, E. & Nordlander, P. Quantum description of the plasmon resonances of a nanoparticle dimer. *Nano Lett.* **9,** 887–891 (2009).
30. Mao, L., Li, Z., Wu, B. & Xu, H. Effects of quantum tunnelling in metal nanogap on surface-enhanced Raman scattering. *Appl. Phys. Lett.* **94,** 243102 (2009).

Acknowledgements

D.N. and D.R.W. acknowledge support from the Robert A. Welch Foundation (grant C-1636) and the Lockheed Martin Advanced Nanotechnology Center of Excellence at Rice (LANCER). F.H. and J.C.C. acknowledge support from the Deutsche Forschungsgemeinschaft, the Baden-Württemberg Stiftung, the European Union through the Bio-Inspired Approaches for Molecular Electronics network (grant MRTN-CT-2006-035859) and the Spanish Ministry of Science and Innovation (Ministerio de Ciencia e Innovacion) (grant FIS2008-04209). F.P. acknowledges funding from a Young Investigator Group.

Author contributions

D.R.W. fabricated the devices, performed all measurements and analysed the data. D.N. supervised and provided continuous guidance for the experiments and the analysis. F.P., F.H. and J.C.C. carried out the theoretical modelling and DFT calculations. The bulk of the paper was written by D.R.W. and D.N. All authors discussed the results and contributed to manuscript revision.

Additional information

The authors declare no competing financial interests. Supplementary information accompanies this paper at www.nature.com/naturenanotechnology. Reprints and permission information is available online at http://npg.nature.com/reprintsandpermissions/. Correspondence and requests for materials should be addressed to D.N.